Monthly Notices
of the
ROYAL ASTRONOMICAL SOCIETY

MNRAS **490,** 1652–1665 (2019)
Advance Access publication 2019 September 7

doi:10.1093/mnras/stz2517

ExoMol molecular line lists XXXVI: $X\,^2\Pi - X\,^2\Pi$ and $A\,^2\Sigma^+ - X\,^2\Pi$ transitions of SH

Maire N. Gorman,[1] Sergei N. Yurchenko[2] and Jonathan Tennyson[2]★

[1]*Department of Physics, Aberystwyth University, Penglais, Aberystwyth, Ceredigion SY23 3BZ, UK*
[2]*Department of Physics and Astronomy, University College London, Gower St, London WC1E 6BT, UK*

Accepted 2019 September 5. Received 2019 September 4; in original form 2019 July 15

ABSTRACT

The GYT line list covering rotational, rovibrational, and rovibronic transitions of the mercapto radical SH is presented. This work extends and replaces the SNaSH line list, which covers the ground (electronic) $X\,^2\Pi$ state only. This extension is prompted by the tentative identification of the ultraviolet features of SH as being of importance in the transmission spectrum of the ultrahot Jupiter exoplanet WASP-121b. This GYT line list model is generated by fitting empirical potential energy, spin–orbit, and electronic angular momenta functions to experimentally measured wavelengths within the $X\,^2\Pi$ and $A\,^2\Sigma^+$ states and to the $A\,^2\Sigma^+ - X\,^2\Pi$ band system using *ab initio* curves as a starting reference point. The fits are compatible with the quoted uncertainty of the experimental data used of ∼0.03–0.3 cm^{-1}. The GYT line list covers wavelengths longer than 0.256 μm and includes 7686 rovibronic states and 572 145 transitions for ^{32}SH. Line lists for the ^{33}SH, ^{34}SH, ^{36}SH, and ^{32}SD isotopologues are generated including a consideration of non-Born–Oppenheimer effects for SD. The line lists are available from the CDS (http://cdsarc.u-strasbg.fr) and ExoMol (www.exomol.com) data bases.

Key words: molecular data – opacity – astronomical data bases: miscellaneous – planets and satellites: atmospheres – stars: low-mass.

1 INTRODUCTION

Previously, we have published line lists for the $X\,^2\Pi$ state of the main isotopologues of the mercapto radical SH (Yurchenko et al. 2018b). Following recent feedback from the exoplanet community, we extend this work to include the $A\,^2\Sigma^+ - X\,^2\Pi$ transitions that feature in the UV region above 0.256 μm.

Recently Evans et al. (2018) used the Space Telescope Imaging Spectrograph (STIS) instrument onboard the *Hubble Space Telescope* (*HST*) to study both primary and secondary transits of the ultrahot Jupiter WASP-121b ($T_{eq} \geq 2500$ K) in the near-infrared (1.15–1.65 μm) regions. Evans et al. observed a steep rise in the opacity from 0.30–0.47 μm in the transmission spectrum of WASP-121b. They postulate that this rise is unlikely to be the result of Rayleigh scattering by H_2 or high-altitude aerosols as this would require an unphysically high temperature. Instead they suggest that it could be due to absorption from the SH radical: previously Zahnle et al. (2009) used a one-dimensional photochemical model to show that the abundances of SH could be enhanced in hot Jupiters due to photolytic and photochemical destruction of H_2S. WASP-121b has been studied in both primary and secondary transits in the near-IR (1.15–1.65 μm) regions. Evans et al. (2018) also note that it is important to identify the species responsible for this ultraviolet (UV) opacity feature as it most likely affects the global energy budget and thermal structure and that the complete characterization of this planet is an ongoing work.

As well as exoplanets, SH is also of interest in AGB (asymptotic giant branch) and Mira variable stars (Yamamura, Kawaguchi & Ridgway 2000), the Sun's atmosphere (Berdyugina & Livingston 2002), and is potentially observable in brown dwarfs (Visscher, Lodders & Fegley 2006). It was also finally detected in the ISM (interstellar medium) by Neufeld et al. (2012) following unsuccessful searches by Meeks, Gordon & Litvak (1969) and Heiles & Turner (1971). It was tentatively detected in comets Halley and IRAS-Araki-Alcook (Krishna Swamy & Wallis 1987, 1988) and more securely subsequently (Kim & Ahearn 1992). Kim & Ahearn (1992) used their analysis of SH in the Comet P/Brorsen-Metcalf (1989) to infer the *g*-factors of the $A - X$ band system. The $A\,^2\Sigma^+ - X\,^2\Pi$ transition of SH has also been detected in translucent interstellar clouds by Zhao et al. (2015), who observed the absorption features at 3242.40 and 3240.66 Å in the $A\,^2\Sigma^+ - X\,^2\Pi$ (0, 0) band. In contrast to Neufeld et al. (2012), they found that their determined abundance of SH to be in line with models for turbulent dissipation regions. On the Earth, the oxidation of H_2S in

★ E-mail: j.tennyson@ucl.ac.uk

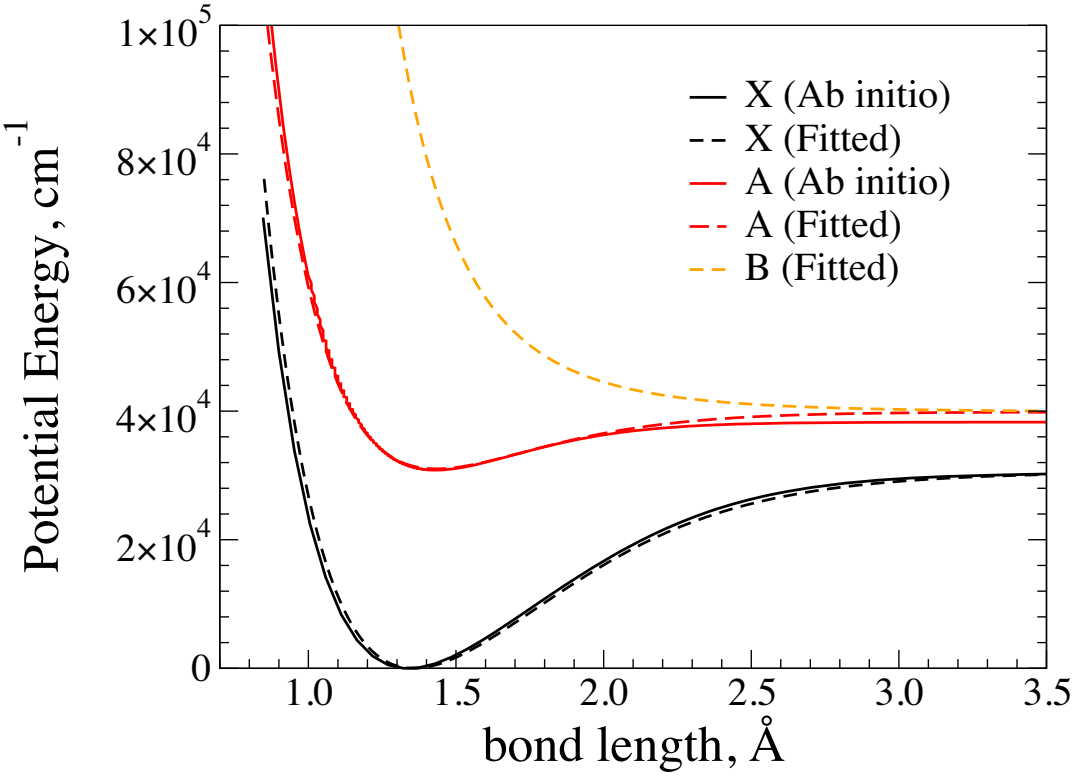

Figure 1. PECs of SH used in the construction of the new extended line list.

the troposphere produces SH, which is a key species in the reactions governing the production of acid rain (Ravichandran, Williams & Fletcher 1994).

The $A\ ^2\Sigma^+ - X\ ^2\Pi$ UV absorption band considered in this work has been detected in both the disc centre and limb of the Sun (Berdyugina & Livingston 2002) in the UV regime using a combination of experimental data of Ramsay (1952) and Ram et al. (1995). Berdyugina & Livingston (2002) synthesized spectra using the model of Grevesse & Sauval (1999) and hence identified five unblended lines around 3300 Å, which they predicted could be useful indicators for determining the S abundances in G and K type stars. However, they noted that strong umbral lines were distorted by stray photospheric light, which prompted Sinha (2015) to revisit the work by applying new models and data in order to understand why SH seemed to appear in the photosphere but not umbral regions. Sinha (2015) concluded that laboratory data on the $A - X$ oscillator strength are essential to resolve the apparent paradox.

The $A\ ^2\Sigma^+$ state of SH has a predissociative character due to its $^2\Sigma^+$ curve crossing repulsive states of symmetry $^2\Sigma^-$, $^4\Sigma^-$, and $^4\Pi$ (Wheeler et al. 1997b), which significantly affects the $A\ ^2\Sigma^+$ lifetimes. The lifetimes of this state of SH and SD were the subject of a number of theoretical and experimental studies (Friedl, Brune & Anderson 1983; Tiee, Ferris & Wampler 1983; Loge & Tiee 1988; Kawasaki et al. 1989; Loge & Tiee 1990; Ubachs & Termeulen 1990; Wheeler, Orr-Ewing & Ashfold 1997a; Wheeler et al. 1997b; Buzaianu et al. 2008).

The spectrum of the mercapto radical SH has been studied experimentally since the work of Glockler & Horwitz (1939) and Lewis & White (1939) with over 100 experimental publications to date. Many of these studies focus on photodissociation, and the hyperfine and magnetically split lines of SH. The spectroscopy of the *A*–*X* band system was studied by Lewis & White (1939) and Ramsay (1952), who undertook flash photolysis experiments using H_2S to produce SH. Lewis & White (1939) were able to measure the $^2\Sigma^+ \leftarrow {}^2\Pi_{3/2}$ system near 3237 Å and calculated spectroscopic constants. Then Ramsay (1952) measured the (0, 0) and (1, 0) bands in absorption and found the latter to be diffuse, indicating predissociation in the first vibrational band of the $A\ ^2\Sigma^+$ state. Later, the (2, 0) band was photographed by Johns & Ramsay (1961). The lifetime of the $v = 0\ A\ ^2\Sigma^+$ state was measured using laser-induced fluorescence (LIF) methods and the Hanle effect by Loge & Tiee (1988). The empirical term values for the *A* state were obtained by Schnieder et al. (1990) from the photodissociation of H_2S at 121.6 nm.

At present, an experimentally limited absorption spectrum line list has been compiled for the $A\ ^2\Sigma^+ - X\ ^2\Pi$ transition of SH by Zahnle et al. (2009) using the RKR potential method of Zare et al. (1973) for the first three vibrational states of the $A\ ^2\Sigma^+$ state. This method uses experimentally derived molecular constants that are subject to errors due to (i) imposing particular Hamiltonians for limiting Hund's cases and (ii) contamination from perturbing electronic states. Here in this work, we bypass molecular constants and instead fit potentials directly to experimentally measured line positions and have thus computed an experimentally tuned theoretical line list that spans higher vibrational and rotational levels as appropriate up to the dissociation limit of the $A\ ^2\Sigma^+$ state.

In this work, we present an accurate and complete line list for SH based on a mixture of *ab initio* calculations and empirical refinements. This line list supersedes the SNaSH line list for SH (Yurchenko et al. 2018b), produced previously as part of the ExoMol project (Tennyson & Yurchenko 2012). The SNaSH line

Table 1. List of experimental data used in refinement of the SH (and SD) $X\,^2\Pi$ and $A\,^2\Sigma^+$ PECs.

Source	No. of transitions	El. Band	Vib. bands	J_{max}
Bernath, Amano & Wong (1983)	50	*X*	(1-0), *X*	11.5
Winkel & Davis (1984)	285	*X*	(1-0), (2-1), (3-2)	34.5
Ram et al. (1995)	175	*X*	(1-0), (2-1), (3-2), (4-3)	16.5
Yamamura et al. (2000)	30	*X*	(1-0), (2-1), (3-2)	25.5
Eliet et al. (2011)	6	*X*	(0-0)	4.5
Martin-Drumel et al. (2012)	70	*X*	(0-0), (1-1)	16.5
Lewis & White (1939)	45	*A*	(0-0)	9.5
Ramsay (1952)	170	*A*	(0-0), (1-0)	12.5
Johns & Ramsay (1961)	146	*A*	(1-0), (2-0)	9.5
Loge & Tiee (1988)	12	*A*	(0-0)	6.5
Ramsay (1952)	189	*A* (SD)	(0-0), (1-0)	15.5
Pathak & Palmer (1969)	21	*A* (SD)	(0-1)	16.5
Johns & Ramsay (1961)	242	*A* (SD)	(1-0), (2-0)	15.5

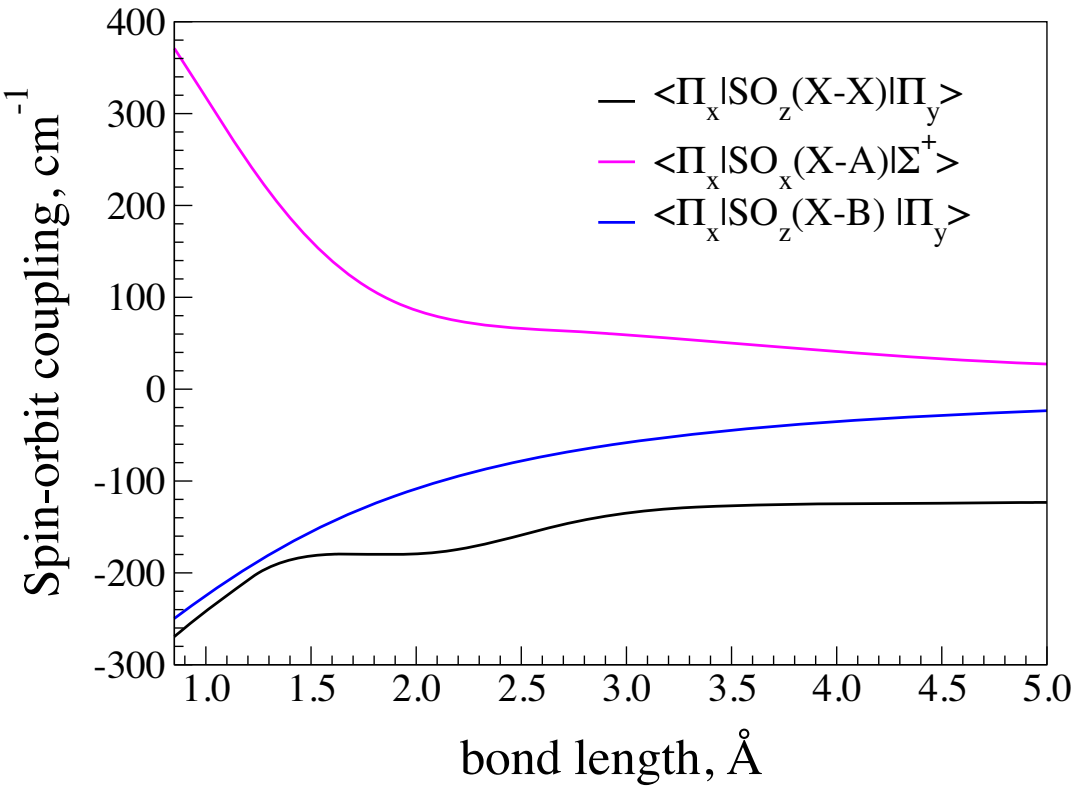

Figure 2. Spin–orbit coupling curves (SOCs) of SH included in the model.

list only considered transitions within the $X\,^2\Pi$ electronic ground state.

2 METHOD

The ExoMol methodology is well established (Tennyson 2012; Tennyson & Yurchenko 2017), so only the key details are given below. The construction of a line list consists of four distinct steps, which are dictated by the Born–Oppenheimer approximation that decouples the Schrödinger equation for a molecule into an electronic Schrödinger equation and rovibronic Schrödinger equation: the former is then used as input to the latter. These distinct steps are:

(i) Calculation of *ab initio* curves by solving the electronic Schrödinger equation to produce potential energy curves (PECs), spin–orbit curves (SOCs), electronic angular momentum curves (EAMCs), dipole moment and transition dipole moment curves (DMCs and TDMCs);

(ii) Refinement of the *ab initio* PECs, SOCs, and EAMCs by fitting to experimental data;

(iii) Solving the rovibronic Schrödinger equation using these refined curves;

(iv) Computing Einstein *A* coefficients using the eigenfunctions obtained and *ab initio* DMCs and TDMCs.

Using MOLPRO (Werner et al. 2012), *ab initio* calculations were performed for low-lying electronic states of SH using a grid of

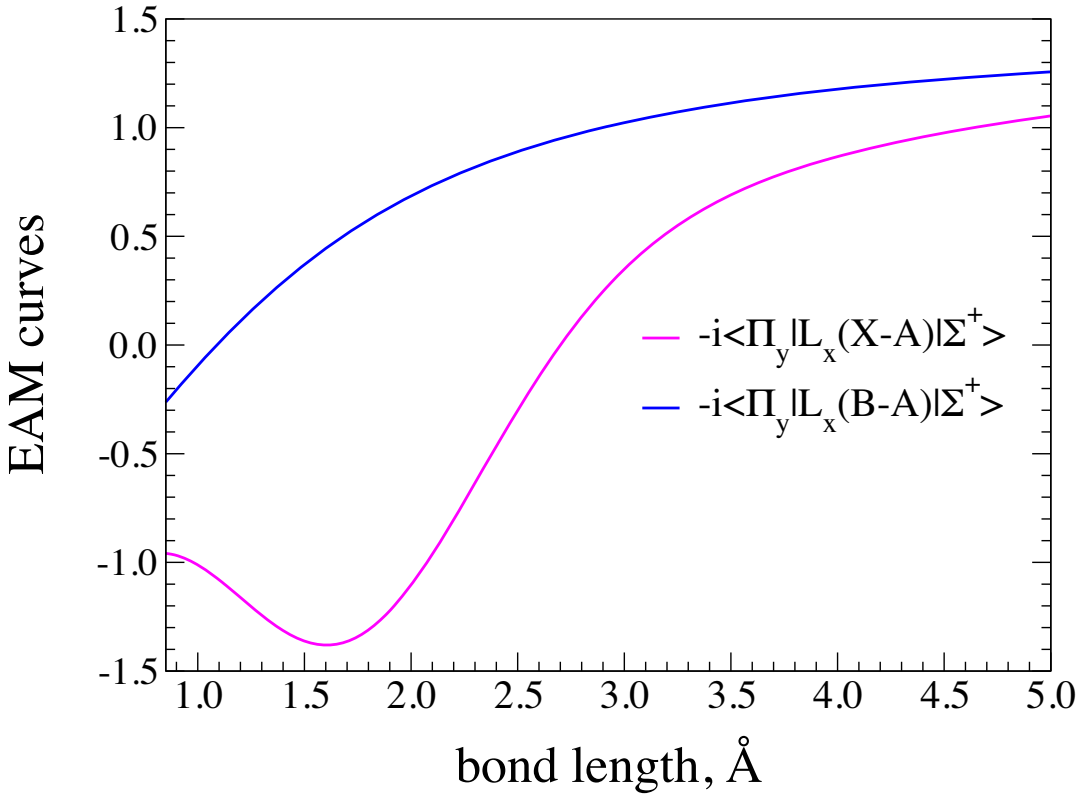

Figure 3. Electronic Angula Momena Curves (EAMCs) of SH included in the model.

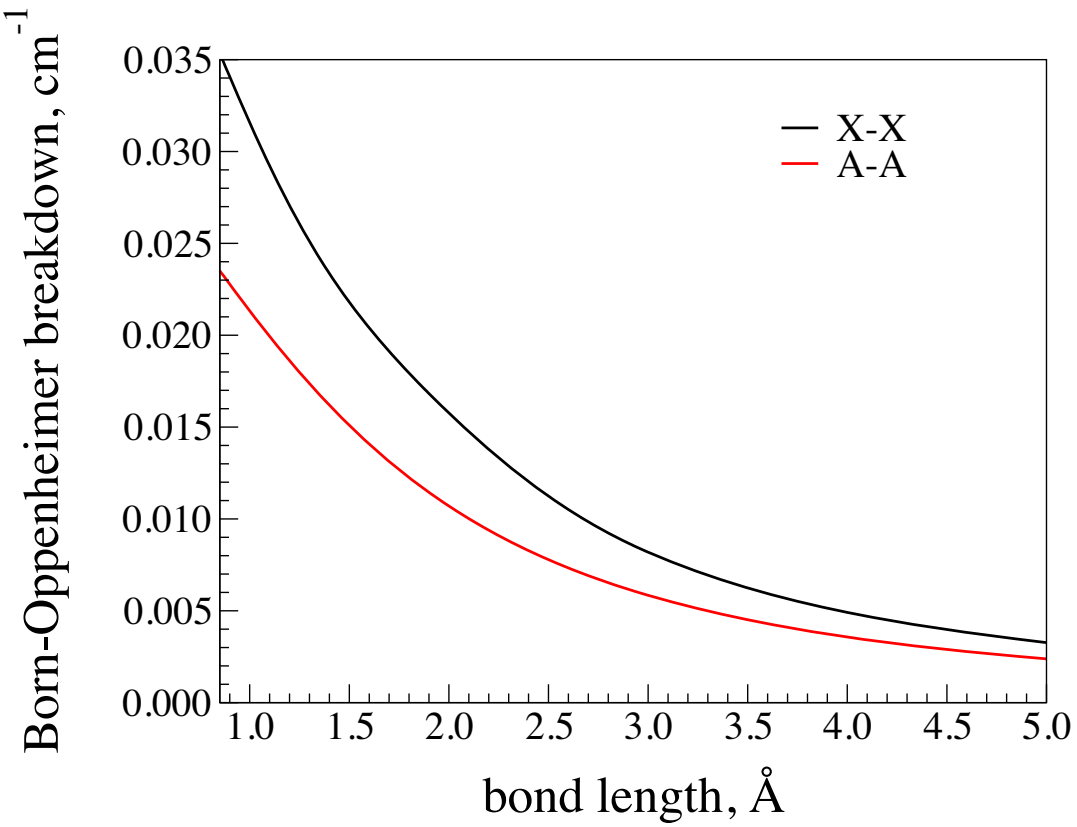

Figure 4. Born–Oppenheimer breakdown curves (BOBCs) of SH included in the model.

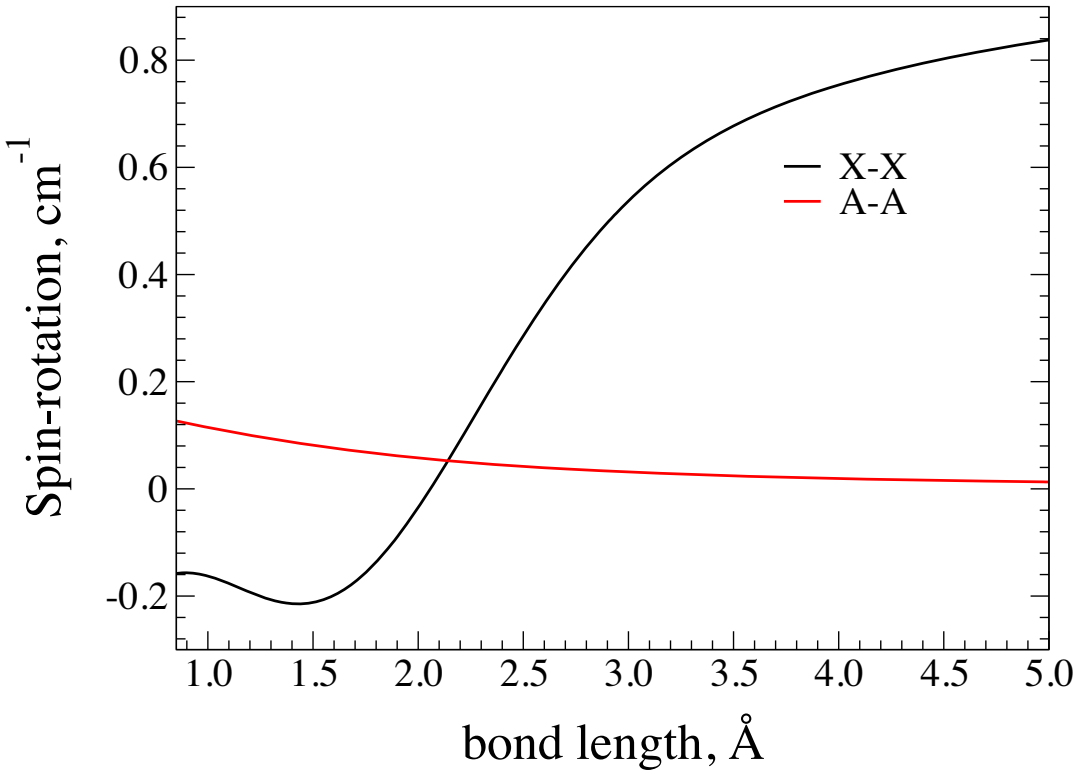

Figure 5. Spin-rotation curves (SRCs) of SH included in the model.

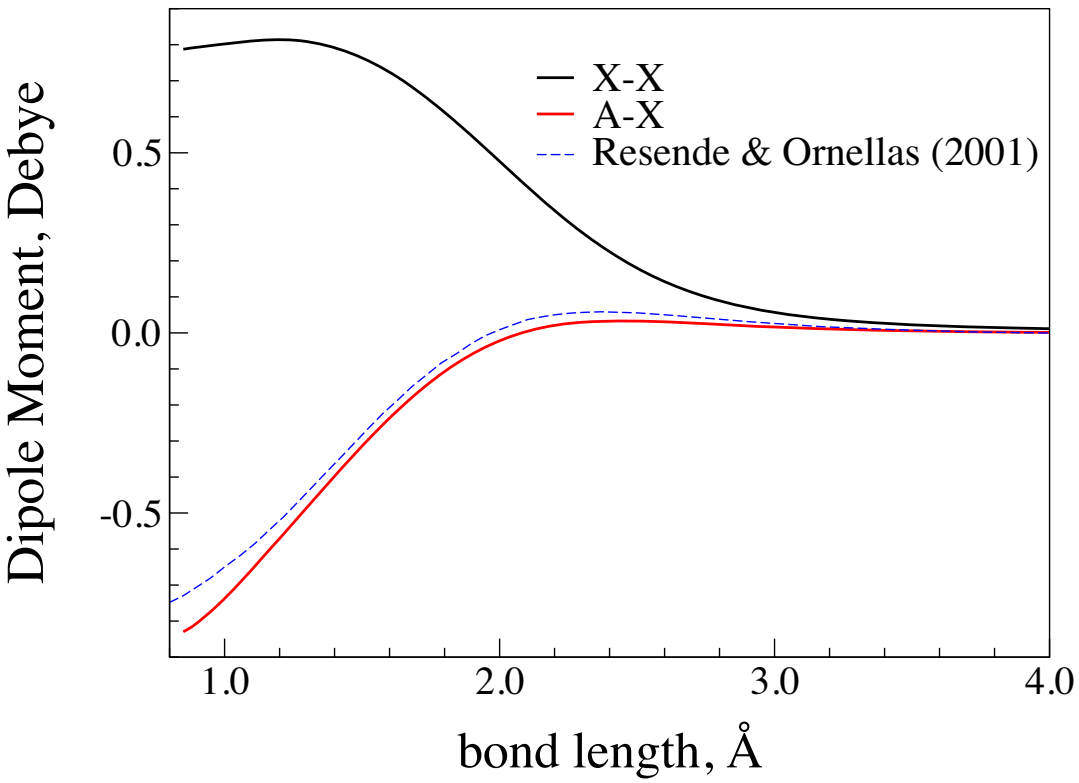

Figure 6. Dipole moment curves (DMCs/TDMCs) *X–X* and *A–X* of SH included in our model. The latter is compared to an *ab initio* TDMC of Resende & Ornellas (2001).

417 points between 0.7 and 19.2 Å with more points concentrated around equilibrium. These calculations included PECs for the $A\,^2\Sigma^+$ and $B\,^2\Pi$ states and the *A*–*X* TDMC and were based on the multireference configuration interaction (MRCI)/aug-cc-pV5Z-DK level of theory (Dunning 1989; Woon & Dunning 1993): the initial complete active space self-consistent field (CASSCF) calculation over which the configuration interaction calculations were built was for the $X\,^2\Pi$ state only. Fig. 1 shows the selection of PEC curves used in the final line list model. The active space was selected to be (8,4,4,1) with (3,1,1,0) closed orbitals. The Douglass–Kroll relativistic corrections were taken into account (kroll = 1).

Yurchenko et al. (2018b) fitted the $X\,^2\Pi$ ground electronic state of SH to available experimental data. Table 1 shows the experimental sources used in this work to fit both the $X\,^2\Pi$ and $A\,^2\Sigma^+$ electronic states.

Despite the experimental interest of SH, there is a dearth of experimentally measured rovibronic transitions required for refinement of the $A\,^2\Sigma^+$–$X\,^2\Pi$ system. As for any electronic transition system, the accuracy of a line list model generated is dependent upon (i) the vibrational and rotational coverage of available experimentally measured line positions and (ii) the measurement accuracy, which is experimentally possible for the wavenumber range where the system is located. Here we are unfortunately limited to four experimental sources (Lewis & White 1939; Ramsay 1952; Johns & Ramsay 1961; Loge & Tiee 1988), which only span the (0, 0), (1, 0), (2,0) *A*–*X* vibronic bands with rotational coverage up to $J = 12.5$. These bands occur at ∼31 000 cm^{-1} (0.32 μm) and have a quoted experimentally measured accuracy of ≈0.1–0.5 cm^{-1}. We do not use the work of Schnieder et al. (1990), which contains empirical vibronic $A\,^2\Sigma^+$ term values ($v = 0...4$, $N = 0...40$) as these are not sufficiently accurate for this study: Schnieder et al. compared their term values to those determined using theoretical extended Rydberg and Morse potentials and calculated discrepancies of ∼1–66 cm^{-1}. More pertinently, these term values were obtained via fitting spectroscopic constants to observed spectra, which hence introduces potential error due to the effect of nearby coupling states.

In order to fit the $A\,^2\Sigma^+$ state PEC, the experimental frequencies were collected from Lewis & White (1939), Ramsay (1952), Johns & Ramsay (1961), and Loge & Tiee (1988), all representing the *A*–*X* transitions, the (0,0), (1,0), and (2,0) vibronic bands (see Table 1). Including the interactions with other nearby lying electronic states is crucial to achieving good reproduction of the experimental frequencies. To this end, the SO and EAM couplings with the $X\,^2\Pi$ state were introduced and varied. The latter affected the quality of the *X* energies, which in turn required us to refine our $X\,^2\Pi$ state spectroscopic model (Yurchenko et al. 2018b) in a global fit to the experimental data listed in Table 1. For any refinement, where possible, it is imperative to use measured transitions as opposed to experimentally determined spectroscopic constants in order to account for perturbations due to higher lying electronic states, which are often not explicitly accounted for during the processes of obtaining spectroscopic constants for individual electronic states. The $X\,^2\Pi$ state, however, did not suffice to account for the spin splitting of the $A\,^2\Sigma^+$, and another $^2\Pi$ state, $B\,^2\Pi$, was added. The $B\,^2\Pi$ state has a repulsive PEC and is much closer to $A\,^2\Sigma^+$, see Fig. 1. Our final spectroscopic model thus consists of the following components:

(i) Three fitted PECs, $X\,^2\Pi$, $A\,^2\Sigma^+$, and $B\,^2\Pi$, Fig. 1;
(ii) Three fitted SOCs, *X*–*X*, *X*–*A*, and *A*–*B*, Fig. 2;
(iii) Two fitted EAMCs, *X*–*A* and *A*–*B*, Fig. 3;
(iv) Two fitted Born–Oppenheimer Breakdown curves (BOBCs), *X* and *A*, Fig. 4;
(v) Two fitted spin-rotation curves (SRC), *X* and *A*, Fig. 5;
(vi) Two *ab initio* DMCs, a diagonal *X*–*X* and transition *A*–*X*, Fig. 6.

Fig. 6 compares our *ab initio* TDMC with that from a similar *ab initio* study computed by Resende & Ornellas (2001) using the MRCI/aug-cc-pV5Z level of theory, which shows generally good agreement.

With this model, the rovibronic Schrödinger equation was then solved using the program DUO (Yurchenko et al. 2016). DUO is the custom-built program developed within the ExoMol group for calculating line lists for general, open-shell diatomics represented by arbitrary number of couplings (Tennyson et al. 2016b). The vibrational basis set comprised 120 functions, 40+40+40 for each of the three electronic states *X*, *A*, and *B*, obtained by solving these three independent problems with the Sinc discrete variable representation (DVR) on a grid of 501 points between 0.85 and 5.00 Å (Yurchenko et al. 2016). Note that although the $B\,^2\Pi$ state is dissociative, since DUO can only deal with bound states basis sets, by the nature of Sinc DVR, the corresponding PEC had an effective infinite wall at the right end of the grid. Using this model, we were able to achieve the accuracy of the fit comparable with the quality of the corresponding experimental data, ∼ 0.001–0.01 cm^{-1} for the *X*–*X* line positions and ∼0.05–0.5 cm^{-1} for the *A*–*X* frequencies, see Table 2 and Fig. 7. The final root-mean-square (rms) errors for the *X*–*X* and *A*–*X* transition wavenumber frequencies are 0.06 and 0.3 cm^{-1}, respectively. Following our previous work on SH (Yurchenko et al. 2018b), both the $X\,^2\Pi$ and $A\,^2\Sigma^+$ PECs were represented using an Extended Morse Oscillator (EMO) function (Lee et al. 1999) as given by

$$V(r) = V_e + (A_e - V_e)\left[1 - \exp\left(-\sum_{k=0}^{N} B_k \xi_p^k (r - r_e)\right)\right]^2, \quad (1)$$

where $A_e - V_e = D_e$ is the dissociation energy, A_e is the corresponding asymptote, r_e is an equilibrium distance of the PEC, and ξ_p is the Šurkus variable (Šurkus, Rakauskas & Bolotin 1984) given by

$$\xi_p = \frac{r^p - r_e^p}{r^p + r_e^p} \quad (2)$$

with $V_e = 0$ for the $X\,^2\Pi$ state. The dissociation energy of the $D_e^{(X)}$ of the $X\,^2\Pi$ state was fixed to the *ab initio* value recommended by Csaszar, Leininger & Burcat (2003) of 3.791 eV ($D_0^{(X)} = 3.625$ eV), which agrees well with the experimental value $D_0^{(X)} = 3.62 \pm 0.03$ eV of Continetti, Balko & Lee (1991). The asymptote limit of the $A\,^2\Sigma^+$ state was estimated as and fixed to $D_e^{(X)} + \Delta E(S^1D) = 4.94$ eV with the atomic excitation energy of sulphur $\Delta E^{S(^1D)} = 1.146$ eV as taken from NIST (Kramida et al. 2019).

The repulsive $B\,^2\Pi$ PEC was represented using the following hyperbolic form:

$$V(r) = A_e + \frac{B_6}{r^6},$$

where the asymptote A_e of the $B\,^2\Pi$ state was fixed with the asymptote of the $A\,^2\Sigma^+$ state, $A_e = 4.94$ eV.

Different couplings and corrections between different states were modelled using either the expansion:

$$F(r) = \sum_{k=0}^{N} B_k\, z^k (1 - \xi_p) + \xi_p\, B_\infty, \quad (3)$$

Table 2. Example of Obs. − Calc. residuals, in cm^{-1}, for the $A\,^2\Sigma^+$–$X\,^2\Pi$ transitions of SH. Here $J' = J'' + 1$ with the quantum labels denoting those of the $X\,^2\Pi$ state.

Vibrational band	J	+/−	Ω	Obs.	Calc.	Obs. − Calc.
(0, 0)	0.5	+	0.5	30 481.38	30 481.34	0.04
(0, 0)	1.5	+	1.5	30 931.39	30 931.36	0.03
(0, 0)	2.5	−	− 1.5	30 951.16	30 951.15	0.01
(0, 0)	2.5	+	0.5	30 487.22	30 487.21	0.01
(0, 0)	3.5	+	0.5	30 565.76	30 565.68	0.08
(0, 0)	4.5	−	− 1.5	30 984.57	30 984.60	− 0.03
(0, 0)	4.5	+	0.5	30 481.75	30 481.70	0.05
(0, 0)	5.5	+	0.5	30 585.97	30 585.90	0.07
(0, 0)	6.5	+	1.5	30 881.06	30 881.02	0.04
(0, 0)	7.5	+	0.5	30 594.27	30 594.25	0.02
(0, 0)	8.5	+	0.5	30 436.10	30 436.15	− 0.05
(0, 0)	9.5	−	− 1.5	30 854.66	30 854.65	0.01
(0, 0)	9.5	+	0.5	30 590.45	30 590.47	− 0.02
(0, 0)	11.5	+	1.5	31 030.03	31 030.07	− 0.04
(0, 0)	12.5	+	1.5	30 807.05	30 807.03	0.02
(1, 0)	1.5	−	− 1.5	32 664.21	32 664.13	0.08
(1, 0)	1.5	−	− 1.5	32 664.18	32 664.13	0.05
(1, 0)	2.5	−	− 0.5	32 325.46	32 325.68	− 0.22
(1, 0)	3.5	+	1.5	32 738.06	32 738.34	− 0.28
(1, 0)	4.5	+	0.5	32 250.82	32 250.81	0.01
(1, 0)	4.5	+	1.5	32 656.80	32 656.88	− 0.08
(1, 0)	5.5	−	− 1.5	32 648.45	32 648.38	0.07
(1, 0)	6.5	+	1.5	32 636.85	32 636.76	0.09
(1, 0)	7.5	−	− 1.5	32 622.07	32 621.93	0.14
(1, 0)	7.5	−	− 0.5	32 199.32	32 199.36	− 0.04
(2, 0)	1.5	+	1.5	34 293.20	34 292.73	0.47
(2, 0)	2.5	−	− 1.5	34 304.50	34 304.04	0.46
(2, 0)	2.5	+	0.5	33 848.00	33 848.22	− 0.22
(2, 0)	4.5	+	0.5	33 823.20	33 823.37	− 0.17
(2, 0)	5.5	−	− 1.5	34 213.90	34 214.18	− 0.28
(2, 0)	5.5	−	− 0.5	33 803.50	33 803.39	0.11
(2, 0)	6.5	+	1.5	34 194.10	34 194.64	− 0.54

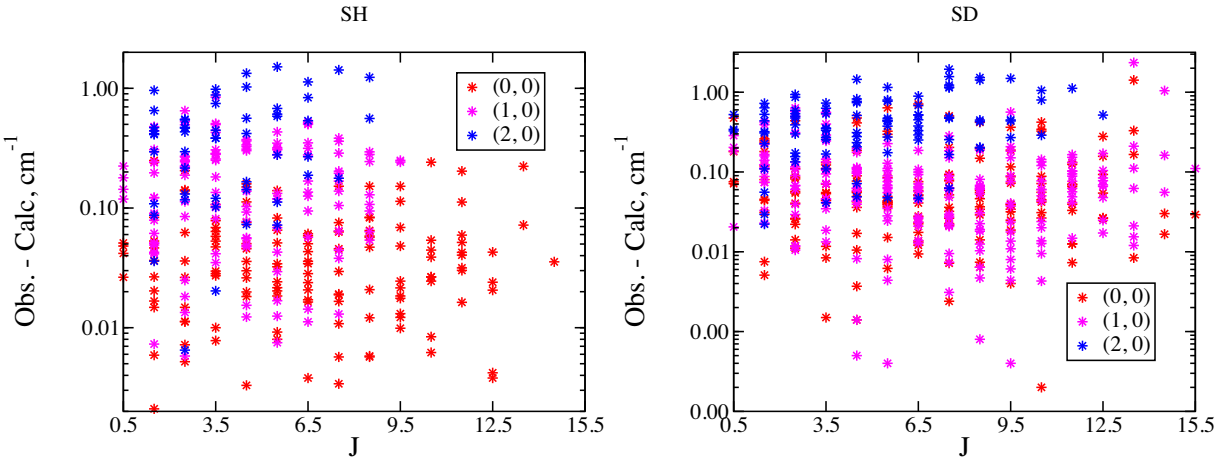

Figure 7. Obs. − Calc. residuals for transitions from the three vibronic bands $A\,^2\Sigma^+$–$X\,^2\Pi$ of SH (left) and SD (right).

where z is either taken as the Šurkus variable $z = \xi_p$ (for A–X EAMC and X, A BOBCs) or using the damped-coordinate polynomial given by (for SOCs, EAMCs A–B, SRCs):

$$z = (r - r_{\rm ref})\, e^{-\beta_2 (r - r_{\rm ref})^2 - \beta_4 (r - r_{\rm ref})^4}, \quad (4)$$

see also Prajapat et al. (2017) and Yurchenko et al. (2018a). Here $r_{\rm ref}$ is a reference position chosen to be close to $r_{\rm e}$ of $X\,^2\Pi$ and β_2 and β_4 are damping factors. In contrast to line positions, which are greatly improved by refining PECs using experimentally measured line positions, this is seldom true for the line intensities, for which DM and TDM curves are usually best computed *ab initio* (Tennyson 2014). The line intensities, which are directly based on the *ab initio* DMCs, often suffer from the numerical noise, especially those from the overtone transitions (Medvedev et al. 2016). In order to

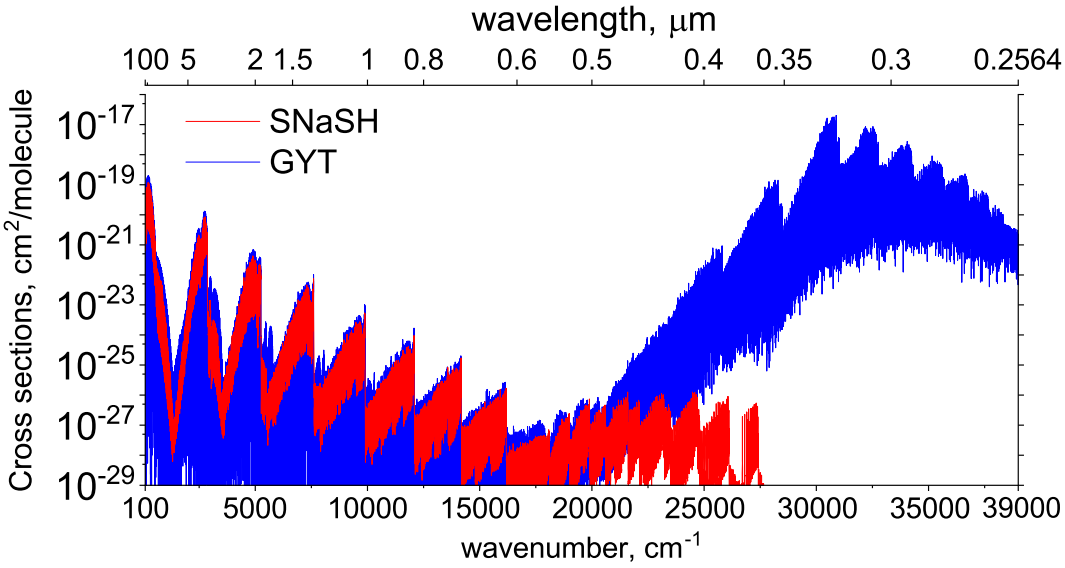

Figure 8. Simulated ^{32}SH absorption spectra at 1500 K for SNaSH (Yurchenko et al. 2018b) and the new GYT line lists. A Gaussian profile of half-width of half-maximum (HWHM) of 1 cm^{-1} was used.

Table 3. Summary statistics for the previous SNaSH (Yurchenko et al. 2018b) and the new GYT line lists for SH.

	Statistics	^{32}SH	^{33}SH	^{34}SH	^{36}SH	^{32}SD
SNaSH	Number of energies	2326	2326	2328	2334	4532
	Number of transitions	81 348	81 274	81 319	81 664	219 463
GYT	Number of energies	7686	7695	7698	7709	12 942
	Number of transitions	572 145	573 299	573 639	575 117	1127 044

reduce this noise, it was sufficient to apply a dipole moment cut-off of 10^{-8} D to the vibrational transition matrix elements, see e.g. Yurchenko et al. (2018c). When computing these matrix elements, the original *ab initio* *X*–*X* and *A*–*X* (T)DMCs were mapped on the DUO grid using the standard cubic spline interpolation technique. The final spectroscopic model in the form of the DUO input file is provided as part of the supplementary data to this paper and can be also found at www.exomol.com. This also includes our fitting set of experimental frequencies.

A sample of the refinement to the data of Ramsay (1952) for the $X\,^2\Pi - A\,^2\Sigma^+$ system is shown in Table 2. The Obs. − Calc. values of the fit are comparable to the actual experimental measurement uncertainty. Although these may seem from the outset to be of much lower accuracy compared to previous ExoMol line lists for non-transition metal-containing diatomics, given that in the regime of ≈30 000 cm^{-1} an uncertainty of 0.5 cm^{-1} corresponds to a resolution R of ≈60 000, which is within the realms of high-spectral resolution methods of characterizing exoplanet atmospheres (Snellen 2004; de Kok et al. 2014).

For all isotopologues of SH-type (^{33}SH, ^{34}SH, ^{36}SH), we use the same empirical model (PECs, SOCs, EAMCs, SRCs, and BOBCs) developed for ^{32}SH. When solving the Schrödinger equation, the mass of sulphur is replaced by the nuclear mass of the corresponding isotope. For the isotopologue ^{32}SD, however, this approach usually leads to too large discrepancies with the experimental line positions. We have therefore refined the ^{32}SH model by fitting to the experimental line positions of ^{32}SD from the *A*–*X* band, which were taken from the same sources listed in Table 1. Ideally, this refinement should be only applied to the BOB-correction. However, due to the lack of the experimental data on the $X\,^2\Pi$ state for SD, we could not build an accurate and self-consistent model without including other curves into the fit. We have therefore varied the parameters of PEC(*A*), PEC (*B*), BOBC (*X*), BOBC (*A*), SRC (*X*), and SRC (*A*) by fitting to the SD line positions from Ramsay (1952), Johns & Ramsay (1961), and Pathak & Palmer (1969). All other curves were fixed to the those from the spectroscopic model of ^{32}SH, including PEC(*X*), SOC (*X*), SOC(*X*–*A*), SOC(*X*–*B*), SOC(*A*–*B*), EAMC(*X*–*A*), and EAMC(*A*–*B*). The rms error of this fit to the *A*–*X* line positions if SD is 0.4 cm^{-1}. The spectroscopic model for SD is included in the supplementary material as a DUO input file.

3 LINE LIST

Using the final spectroscopic model in DUO, line lists (called GYT) for five isotopologues of SH were computed, ^{32}SH, ^{33}SH, ^{34}SH, ^{36}SH, and ^{32}SD. The upper states were truncated at the asymptote A_0 of $A\,^2\Sigma^+$ (∼39 000 cm^{-1}), while the lower states were limited by the dissociation energy of the $X\,^2\Pi$ state D_0 (∼31 000 cm^{-1}). Thus, the GYT line lists cover the wavenumber range up to 39 000 cm^{-1} (>0.256 μm). The ^{32}SH line list contains 7686 *X* and *A* rovibronic states and 572 145 transitions, covering both bands *X*–*X* and *A*–*X*. Our new GYT line lists supersede the SNaSH line lists for SH (Yurchenko et al. 2018b) and extend coverage into the UV regime. Fig. 8 shows a comparison of the new GYT line list with SNaSH. Below 10 000 cm^{-1}, the two line lists agree well; above this, there are difference due to the inclusion of the $A\,^2\Sigma^+$. Besides the strong UV absorption of the $A\,^2\Sigma^+$, there are differences in the $X\,^2\Pi$

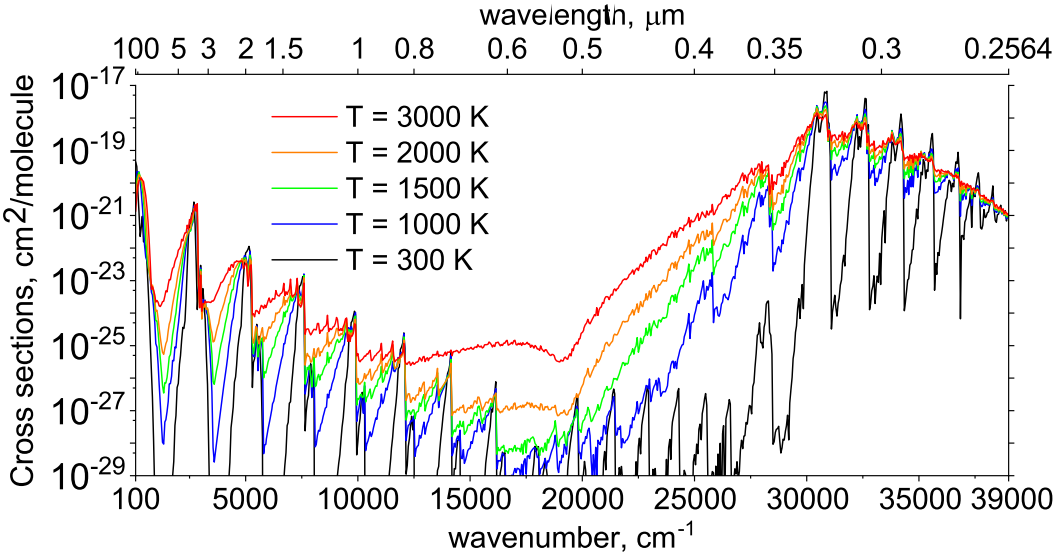

Figure 9. Simulated absorption spectra of ^{32}SH for a range of temperatures; the curves become systematically flatter as T increases. A Gaussian profile of half-width of half-maximum (HWHM) of 1 cm^{-1} was used.

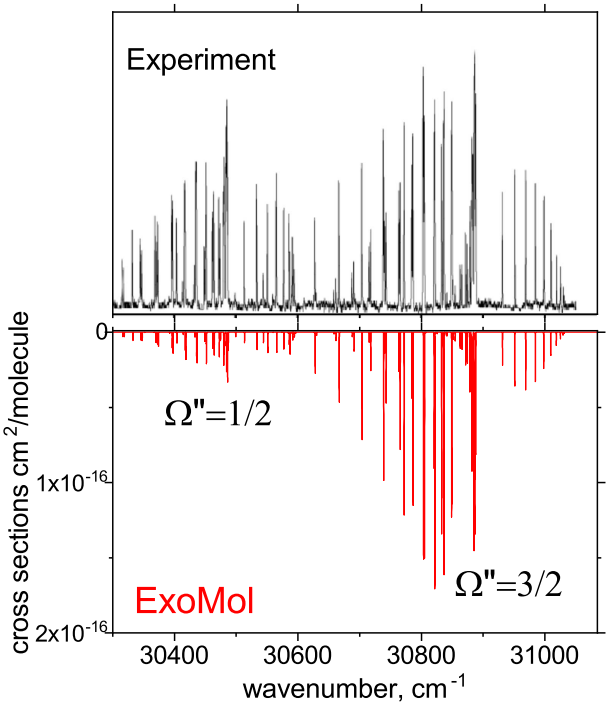

Figure 10. Comparison of the absorption spectra of SH at $T = 1800$ K computed using our line list (Gaussian line profile with an HWHM of 0.1 cm^{-1}) with a laser-induced dispersed fluorescence spectrum of $A\,^2\Sigma^+$–$X\,^2\Pi_{3/2}$ by Tsai & Lin (2010) for the (0, 0) band.

state absorption in the visible. Table 3 showcases the size of the two line lists for the various main isotopologues considered. Fig. 9 shows the temperature dependence of the SH spectra simulated using the EXOCROSS program (Yurchenko, Al-Refaie & Tennyson 2018d). Although the partition functions for the SH isotopologues were updated to include the A state energies, they do not differ significantly from our previous partition functions due to very high energy excitations of those A states.

In order to compare our line list to experimental spectrum, we have used EXOCROSS to simulate spectra from our new extended model. In Figs 10–13, we show comparisons between simulated and experimental spectra. Fig. 14 compares the A–X (0,0) bands of SH and SD at $T = 1750$ K.

4 LIFETIMES

The lifetime of state i, τ_i, can be computed by summing over the A coefficients (Tennyson et al. 2016a):

$$\tau_i = \frac{1}{\sum_f A_{if}}\,. \tag{5}$$

Our values of the lifetimes for the $v = 0$ and 1 vibrational states of ^{32}SH are 449 and 513 ns, respectively. The lifetimes of the A states are strongly affected by the predissociative, forbidden interactions with (at least) one of the three crossing states. Predissociation is not included into our current model and therefore we do not expect the observed lifetimes to be shorter than the ones we compute by simply considering emission lines.

The natural lifetime of the $A\,^2\Sigma^+$ $v = 0$ state has been experimentally measured to be in the range 0.5–2.0 ns by Tiee et al. (1983), and (3 ± 2) ns by Friedl et al. (1983). Ubachs, Termeulen & Dymanus (1983) determined that the natural lifetime decreased monotonically from (3.2 ± 0.3) ns for $N' = 0$ to (0.95 ± 0.02) ns for $N' = 9$. Friedl et al. (1983) also measured the radiative lifetime to be (820 ± 240), ns which they note is comparable to the *ab initio* radiative lifetime calculated by Senekowitsch et al. (1985) of 704 ns. Later, Loge & Tiee (1988) used the Hanle effect and produced an estimate of 0.17–0.30 ns for the $A\,^2\Sigma^+$ $v = 0$ state: this discrepancy with previous estimates was commented on by Ubachs & Termeulen (1990) before Loge & Tiee (1990) provided an explanation in terms of saturation of the transition due to power broadening using a pulsed laser.

The predissociative lifetime of the $A\,^2\Sigma^+$ $v = 1$ state was measured using cavity ringdown spectroscopy experiments by Wheeler et al. (1997b,a), who determined values between 4.08 and 5.45 ps: the authors note that the $A\,^2\Sigma^+$ is sensitive to coupling with nearby dissociative $1^4\Sigma^-$, $1^2\Sigma^-$, and $1^4\Pi$ curves and provide

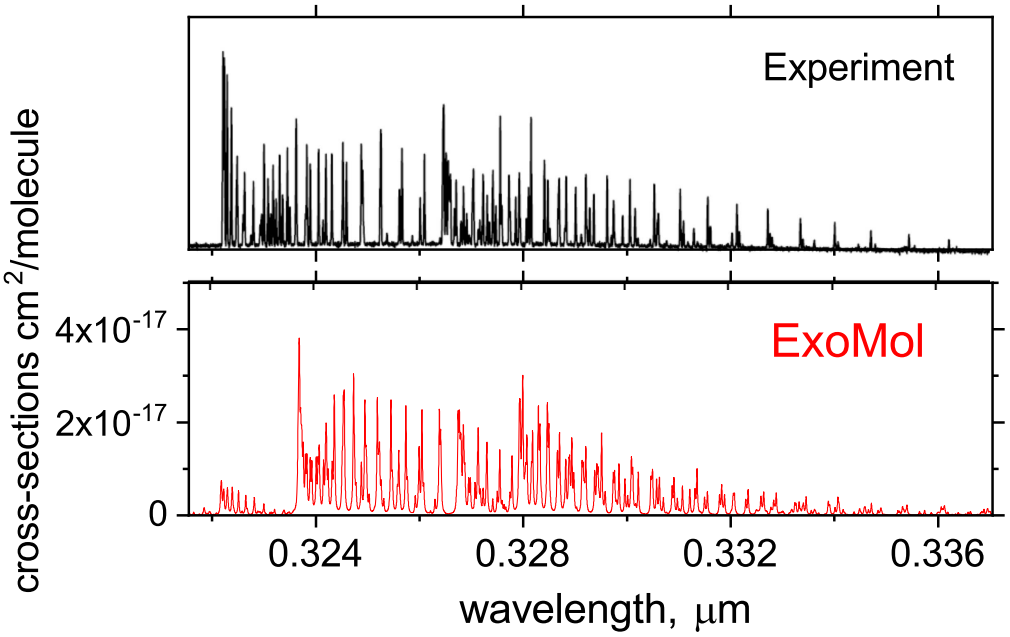

Figure 11. Comparison of the new line list with the experimentally measured spectrum of the (0, 0) *A*–*X* band by Buzaianu et al. (2008) using the cavity ringdown spectroscopy (CRDS). Considering a good agreement of our fit for the (0,0) *A*–*X* band (see Fig. 10), we believe that the shift of ∼0.014 μm can be attributed to a calibration problem in the experimental data.

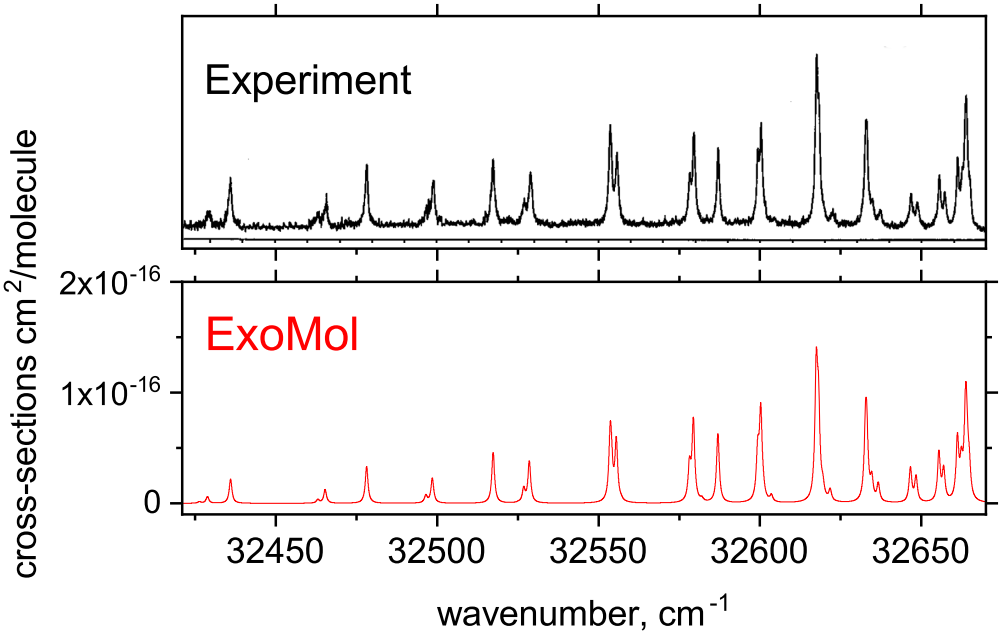

Figure 12. Comparison of the absorption spectra ($T = 300$ K) computed using our line list with the cavity ringdown spectroscopy (CRDS) spectrum recorded by Wheeler et al. (1997b) for the (1, 0) *A*–*X* band. A Voigt profile with $\gamma = 0.5$ cm^{-1} was used.

a comprehensive explanation of why their estimates are ∼5 orders of magnitude smaller than complementary measurements of natural and radiative lifetime.

Using our vibrationally averaged transition dipole moment $\bar{\mu}_{00} = \langle X|\mu|A\rangle = 0.340$ D, we obtain the corresponding (0,0) *A*–*X* Einstein coefficient $A_{00} = 1.026 \times 10^{-6}$ 1/s and oscillator strength $f_{00} = 0.0017$, where the following definition of the vibrational Einstein A coefficient was used:

$$A_{fi}^{(J=0)} = \frac{64 \times 10^{-36} \pi^4 (\nu_{00})^3}{3h} \bar{\mu}_{00}^2. \quad (6)$$

This can be compared to the oscillator strength values $f_{00} = 0.0022$ by Berdyugina & Livingston (2002) (solar spec-

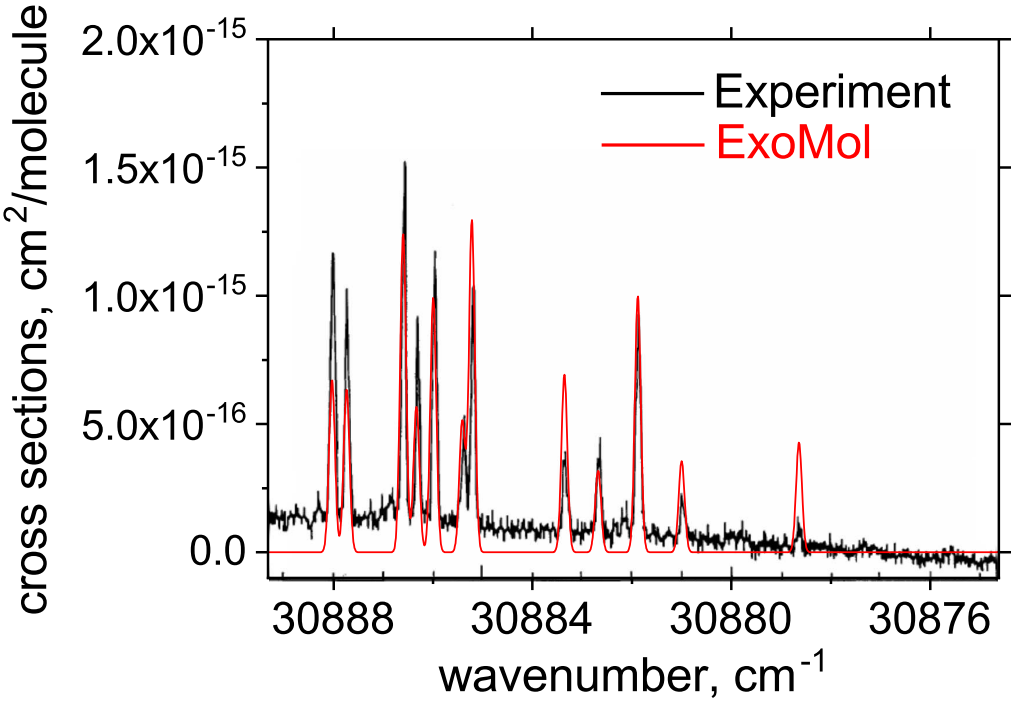

Figure 13. Comparison of the absorption spectra of SH at $T = 300$ K computed using our line list with the LIF excitation spectrum of the $A\,^2\Sigma^+$–$X\,^2\Pi_{3/2}$ by Loge & Tiee (1988) for the (0, 0) A–X band. A Gaussian line profile with the HWHM of 0.07 cm^{-1} was used.

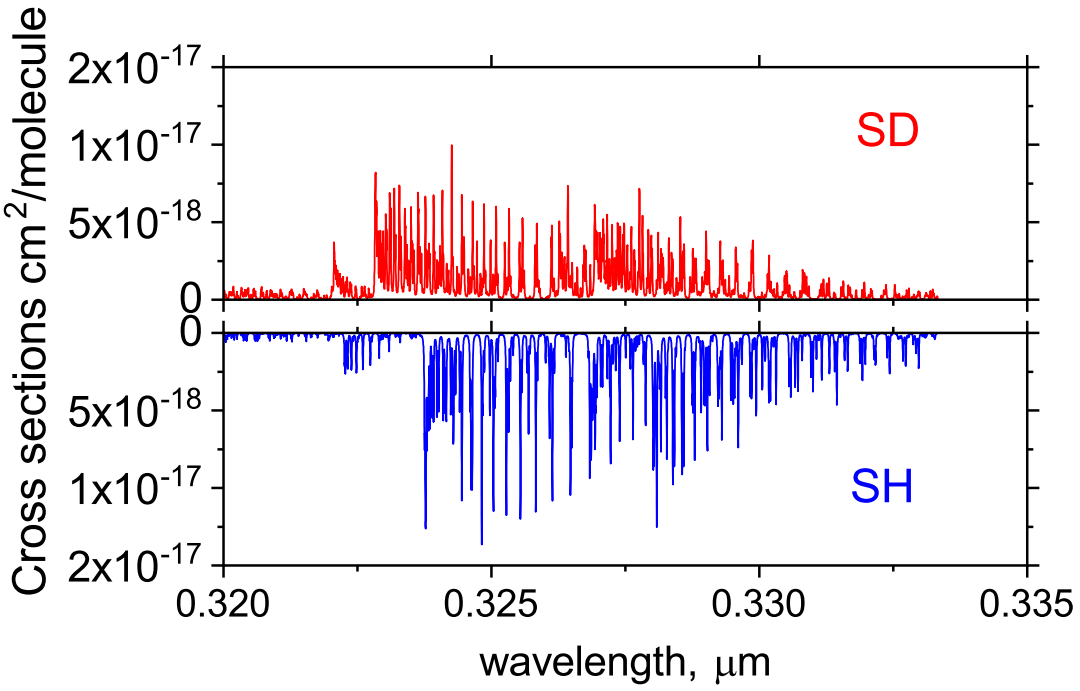

Figure 14. Comparison of the A–X (0, 0) absorption spectra ($T = 1750$ K) of SH and SD generated using our line list and the Voigt line profile with $\gamma = 0.5$ cm^{-1} and assuming no abundance factors.

Table 4. Extract from the states file of the $^{32}S^{1}H$ line list.

i	Energy (cm^{-1})	g_i	J	τ	g-factor	Parity	e/f	State	v	Λ	Σ	Ω
222	32 632.921 24	8	1.5	5.1332E-07	0.667 40	–	e	A2Sigma+	1	0	−0.5	−0.5
223	32 720.908 55	8	1.5	8.1317E-02	−0.014 13	–	e	X2Pi	28	−1	0.5	−0.5
224	32 943.515 85	8	1.5	1.0814E-01	0.814 77	–	e	X2Pi	29	−1	−0.5	−1.5
225	33 233.900 92	8	1.5	1.0856E-01	−0.014 40	–	e	X2Pi	29	−1	0.5	−0.5
226	33 482.050 87	8	1.5	1.4501E-01	0.815 03	–	e	X2Pi	30	−1	−0.5	−1.5
227	33 773.825 78	8	1.5	1.4573E-01	−0.014 67	–	e	X2Pi	30	−1	0.5	−0.5
228	34 046.798 57	8	1.5	1.6400E-01	0.815 27	–	e	X2Pi	31	−1	−0.5	−1.5
229	34 221.198 40	8	1.5	5.8938E-07	0.667 39	–	e	A2Sigma+	2	0	−0.5	−0.5
230	34 339.878 91	8	1.5	1.6466E-01	−0.014 92	–	e	X2Pi	31	−1	0.5	−0.5
231	34 637.045 39	8	1.5	1.5672E-01	0.815 50	–	e	X2Pi	32	−1	−0.5	−1.5
232	34 931.356 80	8	1.5	1.5718E-01	−0.015 16	–	e	X2Pi	32	−1	0.5	−0.5
233	35 252.162 94	8	1.5	1.4828E-01	0.815 73	–	e	X2Pi	33	−1	−0.5	−1.5
234	35 547.638 21	8	1.5	1.4862E-01	−0.015 39	–	e	X2Pi	33	−1	0.5	−0.5
235	35 601.523 44	8	1.5	6.8906E-07	0.667 36	–	e	A2Sigma+	3	0	−0.5	−0.5
236	35 891.592 74	8	1.5	1.5436E-01	0.815 95	–	e	X2Pi	34	−1	−0.5	−1.5
237	36 188.171 16	8	1.5	1.5475E-01	−0.015 61	–	e	X2Pi	34	−1	0.5	−0.5
238	36 554.834 99	8	1.5	1.8246E-01	0.816 17	–	e	X2Pi	35	−1	−0.5	−1.5
239	36 758.866 98	8	1.5	8.3812E-07	0.667 29	–	e	A2Sigma+	4	0	−0.5	−0.5
240	36 852.464 55	8	1.5	1.8357E-01	−0.015 83	–	e	X2Pi	35	−1	0.5	−0.5
241	37 241.440 04	8	1.5	2.4394E-01	0.816 38	–	e	X2Pi	36	−1	−0.5	−1.5
242	37 540.078 57	8	1.5	2.4736E-01	−0.016 04	–	e	X2Pi	36	−1	0.5	−0.5
243	46.129 449	12	2.5	1.9375E+02	0.385 73	+	e	X2Pi	0	1	0.5	1.5
244	445.285 462	12	2.5	4.0720E+01	−0.042 73	+	e	X2Pi	0	1	−0.5	0.5
245	2642.838 347	12	2.5	6.8587E-01	0.384 56	+	e	X2Pi	1	1	0.5	1.5
246	3041.672 932	12	2.5	6.6743E-01	−0.041 56	+	e	X2Pi	1	1	−0.5	0.5

Notes. i: State counting number.
$\tilde{E}$: State energy in cm^{-1}.
g_i: Total statistical weight, equal to $g_{ns}(2J + 1)$.
J: Total angular momentum.
τ: Lifetime (s^{-1}).
g: Landé g-factors.
+/ −: Total parity.
e/f: Rotationless parity.
State: Electronic state.
v: State vibrational quantum number.
Λ: Projection of the electronic angular momentum.
Σ: Projection of the electronic spin.
Ω: Projection of the total angular momentum, $\Omega = \Lambda + \Sigma$.

trum) and $f_{00} = 0.0029$ by Resende & Ornellas (2001) (*ab initio*).

The predissociation of the $A\,^2\Sigma^+$ states is mainly attributed to the interaction with $1^4\Sigma^-$. The $A\,^2\Sigma^+$ state vibrational levels of the SD molecule, however are less affected by this interaction (Wheeler et al. 1997a). The experimental, collision-free lifetime reported by Tiee et al. (1983) ($v = 0$) is 189 ns. The DUO value is 438 ns.

Using the ExoMol format described by Tennyson et al. (2016c), a sample of the GYT states file is shown in Table 4 and a sample of the GYT transitions file is shown in Table 5.

5 CONCLUSIONS

We extend the previous ExoMol line list that covered only the $X\,^2\Pi$ state of the mercapto (SH) to include transitions within the $A\,^2\Sigma^+ - X\,^2\Pi$ system. This new experimentally tuned theoretical line list, GYT, supersedes the previous ExoMol SNaSH line list (Yurchenko et al. 2018b) and the existing experimental, limited, absorption-spectrum line list of Zahnle et al. (2009), which has previously been successfully used to model Hot Jupiters. Using available experimental data, we have generated a model for SH and a separate model for SD. These new line lists now extend out into the UV regime (>0.256 μm) and cover transitions up to ∼39 000 cm^{-1}.

As with all line lists produced by the ExoMol, the validity of models is dependent on the vibrational and, to a lesser extent, rotational ranges of experimental data: here we have been limited to $v' \leq 2$. Using the custom-built DUO programme, an array of coupling contributions have been included to account for nearby dissociative electronic states and higher order breakdown terms. The accuracy of models is also dependent on the underlying measurement uncertainties of available experimental data: here high-level *ab initio* curves have been refined to accuracies similar to the available experimental data (∼0.3 cm^{-1}). These line lists are available from the CDS http://cdsarc.u-strasbg.fr and ExoMol www.exomol.com data bases. States files are provided as part of the supplementary material to this paper together with the spectroscopic models in the form of the DUO input files.

The spectral range and accuracy of our line lists taken together correspond to a resolving power ∼60 000, hence making these line lists of use within the developing research niche of using high-resolution planetary radial velocity measurements to characterize exoplanetary atmospheres. At present, the ExoMol

Table 5. Extract from the transitions file of the ^{32}SH line list.

f	i	A_{fi} (s^{-1})	$\tilde{\nu}_{fi}$
3438	3157	6.6514E-05	30 001.408 693
1314	1188	1.7677E-07	30 002.099 401
365	85	4.7787E-07	30 002.250 973
286	164	4.5799E-07	30 002.276 822
716	407	5.7148E-07	30 002.319 009
637	486	4.8517E-06	30 002.383 604
2110	1966	1.4836E+05	30 002.561 088
2396	2418	1.0166E-05	30 002.770 705
2859	2866	2.3905E-05	30 003.312 455
1781	1655	4.3074E-08	30 003.351 508
1729	1891	4.0626E-07	30 003.584 108
1704	1732	1.1467E-10	30 004.141 218
380	403	1.4745E+05	30 004.344 227
1803	1659	1.4449E-09	30 004.767 420
3367	3229	6.6557E-05	30 005.009 831
708	406	4.9356E-06	30 005.192 773
538	403	2.0426E+05	30 005.269 387

Notes. f: Upper state counting number;
i: Lower state counting number;
A_{fi}: Einstein-*A* coefficient in s^{-1};
$\tilde{\nu}_{fi}$: transition wavenumber in cm^{-1}.

group has published several line lists that, owing to required experimental data been available, could be of use for this method including most recently TiO (McKemmish et al. 2019). In order to produce such a line list of this desired accuracy, the MARVEL process (Furtenbacher, Császár & Tennyson 2007) can be used to generate what can be regarded as an 'experimental' list of rovibronic energies from measured transitions. This process has already been used for various molecules of interest in exoplanets and cool stellar objects including ZrO (McKemmish et al. 2018), TiO (McKemmish et al. 2017), C_2 (Furtenbacher et al. 2016), C_2H_2 (Chubb et al. 2018a), H_2S (Chubb et al. 2018b), NH_3 (Al Derzi et al. 2015), and most recently NH (Darby-Lewis et al. 2019).

Our new extended line list has the benefit of having the required *accuracy* for use in high-resolution spectroscopy and the relative property of *completeness* (up to ∼5000 K) owing to its extended spectral range. We envisage this will help benefit the characterization of hot Jupiter exoplanets such as WASP-121b in which SH is suspected to contribute to opacity within the UV regime.

ACKNOWLEDGEMENTS

This work was supported by the UK Science and Technology Research Council (STFC) No. ST/R000476/1. This work made extensive use of UCL's Legion high-performance computing facility along with the STFC DiRAC HPC facility supported by BIS National E-infrastructure capital grant ST/J005673/1 and STFC grants ST/H008586/1 and ST/K00333X/1. Some support was provided by the NASA Laboratory Astrophysics program.

REFERENCES

Al Derzi A. R., Furtenbacher T., Tennyson J., Yurchenko S. N., Császár A. G., 2015, J. Quant. Spectrosc. Radiat. Transfer, 161, 117
Berdyugina S. V., Livingston W. C., 2002, A&A, 387, L6
Bernath P. F., Amano T., Wong M., 1983, J. Mol. Spectrosc., 98, 20
Buzaianu M.-D., Makarov V. I., Morell G., Weiner B. R., 2008, Chem. Phys. Lett., 455, 26
Chubb K. L. et al., 2018a, J. Quant. Spectrosc. Radiat. Transfer, 204, 42
Chubb K. L. et al., 2018b, J. Quant. Spectrosc. Radiat. Transfer, 218, 178
Continetti R. E., Balko B. A., Lee Y. T., 1991, Chem. Phys. Lett., 182, 400
Csaszar A. G., Leininger M. L., Burcat A., 2003, J. Phys. Chem. A, 107, 2061
Darby-Lewis D. et al., 2019, J. Mol. Spectrosc., 362, 69
de Kok R. J., Birkby J., Brogi M., Schwarz H., Albrecht S., de Mooij E. J. W., Snellen I. A. G., 2014, A&A, 561, A150
Dunning T. H., 1989, J. Chem. Phys., 90, 1007
Eliet S., Martin-Drumel M.-A., Guinet M., Hindle F., Mouret G., Bocquet R., Cuisset A., 2011, J. Mol. Spectrosc., 1006, 13
Evans T. M. et al., 2018, AJ, 156, 283
Friedl R. R., Brune W. H., Anderson J. G., 1983, J. Chem. Phys., 79, 4227
Furtenbacher T., Császár A. G., Tennyson J., 2007, J. Mol. Spectrosc., 245, 115
Furtenbacher T., Szabó I., Császár A. G., Bernath P. F., Yurchenko S. N., Tennyson J., 2016, ApJS, 224, 44
Glockler G., Horwitz W., 1939, J. Chem. Phys., 7, 857
Grevesse N., Sauval A.-J., 1999, A&A, 347, 348
Heiles C. E., Turner B. E., 1971, Astrophys. Lett., 8, 89
Johns J. W. C., Ramsay D. A., 1961, Can. J. Phys., 39, 210
Kawasaki M., Sato H., Inoue G., Suzuki M., 1989, J. Chem. Phys., 91, 6758
Kim S. J., Ahearn M. F., 1992, Icarus, 97, 303
Kramida A., Yu. Ralchenko Reader J., NIST ASD Team, 2019, NIST Atomic Spectra Database (Ver. 5.6.1). Natl. Inst. Stand. Technol., Gaithersburg, MD, Available: https://physics.nist.gov/asd (accessed 2019 April 13).
Krishna Swamy K.-S., Wallis M.-K., 1987, MNRAS, 228, 305
Krishna Swamy K.-S., Wallis M. K., 1988, A&AS, 74, 227
Lee E. G., Seto J. Y., Hirao T., Bernath P. F., Le Roy R. J., 1999, J. Mol. Spectrosc., 194, 197
Lewis M. N., White J. U., 1939, Phys. Rev., 55, 894
Loge G. W., Tiee J. J., 1988, J. Chem. Phys., 89, 7167
Loge G. W., Tiee J. J., 1990, J. Chem. Phys., 92, 2122
McKemmish L. K. et al., 2017, ApJS, 228, 15
McKemmish L. K. et al., 2018, ApJ, 867, 33
McKemmish L. K., Masseron T., Hoeijmakers J., Pérez-Mesa V. V., Grimm S. L., Yurchenko S. N., Tennyson J., 2019, MNRAS, 488, 2836
Martin-Drumel M. A., Eliet S., Pirali O., Guinet M., Hindle F., Mouret G., Cuisset A., 2012, Chem. Phys. Lett., 550, 8
Medvedev E. S., Meshkov V. V., Stolyarov A. V., Ushakov V. G., Gordon I. E., 2016, J. Mol. Spectrosc., 330, 36
Meeks M. L., Gordon M. A., Litvak M. M., 1969, Science, 163, 173
Neufeld D. A. et al., 2012, A&A, 542, L6
Pathak C. M., Palmer H. B., 1969, J. Mol. Spectrosc., 32, 157
Prajapat L., Jagoda P., Lodi L., Gorman M. N., Yurchenko S. N., Tennyson J., 2017, MNRAS, 472, 3648
Ramsay D. A., 1952, J. Chem. Phys., 20, 1920
Ram R. S., Bernath P. F., Engleman R., Brault J. W., 1995, J. Mol. Spectrosc., 172, 34
Ravichandran K., Williams R., Fletcher T.-R., 1994, Chem. Phys. Lett., 217, 375
Resende S. M., Ornellas F. R., 2001, Chem. Phys. Lett., 349, 123
Schnieder L., Meier W., Welge K. H., Ashfold M. N. R., Western C. M., 1990, J. Chem. Phys., 92, 7027
Senekowitsch J., Werne H.-J., Rosmus P., Reinsch A., Oneil S.-V., 1985, J. Chem. Phys., 83, 4661
Sinha K., 2015, Sol. Phys., 290, 3257
Snellen I. A. G., 2004, MNRAS, 353, L1
Šurkus A. A., Rakauskas R. J., Bolotin A. B., 1984, Chem. Phys. Lett., 105, 291
Tennyson J., 2012, WIREs Comput. Mol. Sci., 2, 698
Tennyson J., 2014, J. Mol. Spectrosc., 298, 1

Tennyson J., Yurchenko S. N., 2012, MNRAS, 425, 21
Tennyson J., Yurchenko S. N., 2017, Mol. Astrophys., 8, 1
Tennyson J., Hulme K., Naim O. K., Yurchenko S. N., 2016a, J. Phys. B: At. Mol. Opt. Phys., 49, 044002
Tennyson J., Lodi L., McKemmish L. K., Yurchenko S. N., 2016b, J. Phys. B: At. Mol. Opt. Phys., 49, 102001
Tennyson J. et al., 2016c, J. Mol. Spectrosc., 327, 73
Tiee J. J., Ferris M. J., Wampler F. B., 1983, J. Chem. Phys., 79, 130
Tsai P.-Y., Lin K.-C., 2010, Phys. Chem. Chem. Phys., 12, 1162
Ubachs W., Termeulen J. J., 1990, J. Chem. Phys., 92, 2121
Ubachs W., Termeulen J. J., Dymanus A., 1983, Chem. Phys. Lett., 101, 1
Visscher C., Lodders K., Fegley Jr. B., 2006, ApJ, 648, 1181
Werner H.-J., Knowles P. J., Knizia G., Manby F. R., Schütz M., 2012, WIREs Comput. Mol. Sci., 2, 242
Wheeler M. D., Orr-Ewing A. J., Ashfold M. N. R., 1997a, J. Chem. Phys., 107, 7591
Wheeler M. D., Orr-Ewing A. J., Ashfold M. N. R., Ishiwata T., 1997b, Chem. Phys. Lett., 268, 421
Winkel R. J., Davis S. P., 1984, Can. J. Phys., 62, 1420
Woon D. E., Dunning T. H., 1993, J. Chem. Phys., 98, 1358
Yamamura I., Kawaguchi K., Ridgway S. T., 2000, ApJ, 528, L33
Yurchenko S. N., Lodi L., Tennyson J., Stolyarov A. V., 2016, Comput. Phys. Commun., 202, 262
Yurchenko S. N., Sinden F., Lodi L., Hill C., Gorman M. N., Tennyson J., 2018a, MNRAS, 473, 5324
Yurchenko S. N., Bond W., Gorman M. N., Lodi L., McKemmish L. K., Nunn W., Shah R., Tennyson J., 2018b, MNRAS, 478, 270
Yurchenko S. N., Williams H., Leyland P. C., Lodi L., Tennyson J., 2018c, MNRAS, 479, 1401
Yurchenko S. N., Al-Refaie A. F., Tennyson J., 2018d, A&A, 614, A131
Zahnle K., Marley M. S., Freedman R. S., Lodders K., Fortney J. J., 2009, ApJ, 701, L20
Zare R. N., Schmeltekopf A. L., Harrop W. J., Albritton D. L., 1973, J. Mol. Spectrosc., 46, 37
Zhao D., Galazutdinov G.-A., Linnartz H., Krełowski J., 2015, A&A, 579, L1

SUPPORTING INFORMATION

Supplementary data are available at *MNRAS* online.

SI.zip

Please note: Oxford University Press is not responsible for the content or functionality of any supporting materials supplied by the authors. Any queries (other than missing material) should be directed to the corresponding author for the article.

This paper has been typeset from a TEX/LATEX file prepared by the author.